Supplementary information for “Negative DEP traps for Single Cell Immobilisation”

The appendices in the supplementary information provide additional information on the construction of the device, the fluid flow analysis used in the paper and a comprehensive set of numerical simulations on the design of the ring array and what assumptions are justified in those numerical simulations.

A Images and photographs of device

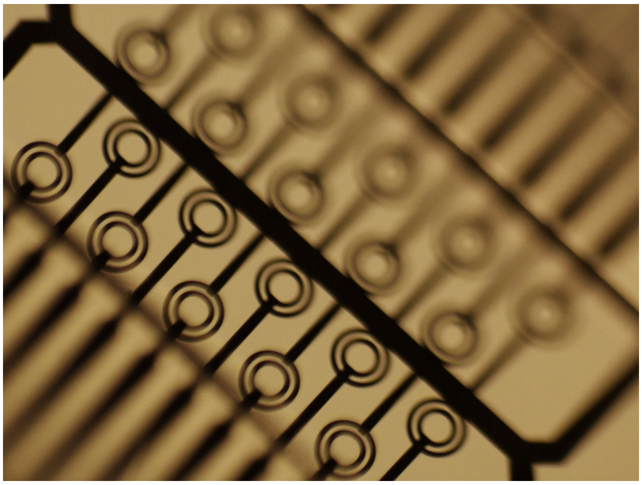

Photograph of a 20 electrode array of ring traps

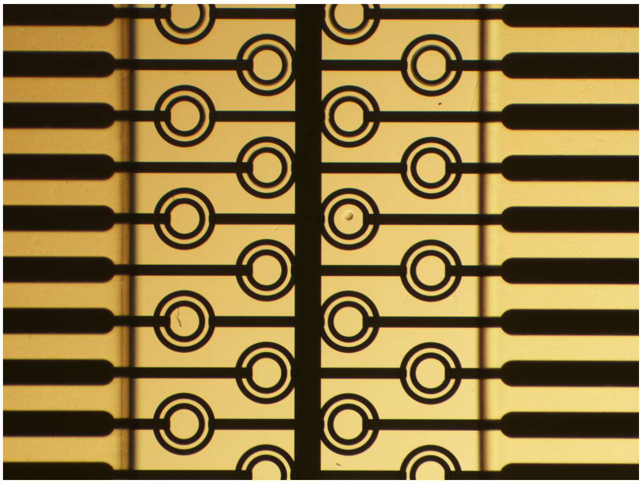

Still image of the array with a single trap activated and holding a cell

B Fourier Series analysis of fluid flow

In two dimensions, the Navier-Stokes Equation reduces to Stokes' equation in the steady state and then to Poisson's equation:

$$\rho_m \frac{\partial \mathbf{u}}{\partial t} + \rho_m (\mathbf{u}\cdot\nabla)\mathbf{u} = -\nabla p + \eta \nabla^2 \mathbf{u} + \boldsymbol{f}$$

$$\boldsymbol{f} = 0, \frac{\partial \mathbf{u}}{\partial t} = 0, \frac{\partial \mathbf{u}}{\partial x} = 0, \frac{\partial p}{\partial y} = \frac{\partial p}{\partial z} = 0$$

$$\Rightarrow \nabla^2 \mathbf{u} = \frac{1}{\eta}\frac{\partial p}{\partial x}$$

or

$$\frac{\partial^2 u_x}{\partial y^2} + \frac{\partial^2 u_x}{\partial z^2} = \Omega, \text{ where } \Omega = \frac{1}{\eta}\frac{\partial p}{\partial x}$$

This gives the velocity along the channel, *u*, as a function of width in the *y*-direction and height in the *z*-direction. This can be solved for a rectangular channel of width *d* and height *h* with a Fourier Series expansion

$$\begin{aligned} u_x &= \sum_{n=1}^{\infty}\sum_{m=1}^{\infty} a_{nm}(\sin ny + \cos ny)(\sin mz + \cos mz) \\ &= \sum_{n=1}^{\infty}\sum_{m=1}^{\infty} a_{nm}(\sin ny)(\sin mz) \end{aligned}$$

Applying the boundary conditions for the rectangular channel:

$$\begin{aligned} &u_x = 0 \ @ \ y = 0, \ z = 0 \\ &\Rightarrow \cos ny = 0 \ \text{ and } \ \cos mz = 0 \end{aligned}$$

and

$$u_x = 0 \ @ \ y = d \text{ or } z = h$$

$$\Rightarrow \begin{cases} nd = k\pi \ \text{ where } \ k = 1,2,3,... \ \Rightarrow n = \dfrac{k\pi}{d} \\ mh = l\pi \ \text{ where } \ l = 1,2,3,... \ \Rightarrow m = \dfrac{l\pi}{h} \end{cases}$$

Giving

$$u_x = \sum_{k=1}^{\infty}\sum_{l=1}^{\infty} a_{kl}\left(\sin\frac{k\pi}{d}y\right)\left(\sin\frac{l\pi}{h}z\right)$$

As a result,

$$\Omega = \frac{\partial^2 u_x}{\partial y^2} + \frac{\partial^2 u_x}{\partial z^2} = -\left[\left(\frac{k\pi}{d}\right)^2 + \left(\frac{l\pi}{h}\right)^2\right]u_x$$

$$\Rightarrow \ \therefore u_x = \frac{-\Omega}{\left[\left(\frac{k\pi}{d}\right)^2 + \left(\frac{l\pi}{h}\right)^2\right]}$$

Then

$$\begin{aligned} &\int_0^d\int_0^h u \sin\frac{p\pi y}{d}\sin\frac{q\pi z}{h}\,dydz \\ &= \sum_{k=1}^{\infty}\sum_{l=1}^{\infty}\int_0^d\int_0^h a_{kl}\left(\sin\frac{k\pi}{d}y\right)\left(\sin\frac{p\pi}{d}y\right)\left(\sin\frac{l\pi}{h}z\right)\left(\sin\frac{q\pi}{h}z\right)dydz \end{aligned}$$

and

$$\left[\int_0^d\int_0^h u \sin\frac{p\pi y}{d}\sin\frac{q\pi z}{h}\,dydz\right]^{\text{p,q odd}} = \frac{4dh}{pq\pi^2}u$$

$$\left[\int_0^d\int_0^h u \sin\frac{p\pi y}{d}\sin\frac{q\pi z}{h}\,dydz\right]^{\text{p,q even}} = 0$$

also

$$\left[\int_0^d\int_0^h a_{kl}\sin\frac{k\pi y}{d}\sin\frac{p\pi y}{d}\sin\frac{l\pi z}{h}\sin\frac{q\pi z}{h}\,dydz\right]^{p\neq k \ \text{ or } \ q\neq l} = 0$$

$$\left[\int_0^d\int_0^h a_{kl}\sin\frac{k\pi y}{d}\sin\frac{p\pi y}{d}\sin\frac{l\pi z}{h}\sin\frac{q\pi z}{h}\,dydz\right]^{p=k \ \text{ and } \ q=l} = a_{kl}\frac{dh}{4}$$

$$\therefore \frac{4dh}{pq\pi^2}u = \frac{dh}{4}a_{kl} \ \text{ if } \ p = k, q = l \ \text{ and all odd.}$$

Therefore

$$\begin{aligned} a_{kl} &= \frac{16}{kl\pi^2}u \\ &= \frac{-16}{kl\pi^2}\frac{\Omega}{\left[\left(\frac{k\pi}{d}\right)^2 + \left(\frac{l\pi}{h}\right)^2\right]} \end{aligned}$$

and

$$u = \sum_{k=1,3...}^{\infty}\ \sum_{l=1,3...}^{\infty} a_{kl}\left(\sin\frac{k\pi}{d}y\right)\left(\sin\frac{l\pi}{h}z\right)dydz$$

$$\text{where } \ a_{kl} = \frac{-16}{kl\pi^2}\frac{\Omega}{\left[\left(\frac{k\pi}{d}\right)^2 + \left(\frac{l\pi}{h}\right)^2\right]}$$

C Numerical simulation of ring electrodes

The equations and procedures outlined in this section are taken from the sources given in the reference list at the end. This section to the paper gives complete details of the numerical simulations used to define the operation of the ring traps.

Introduction

In the dipole approximation, the equation for the time averaged dielectrophoretic (DEP) force on a particle in a single frequency harmonic electric field with homogeneous phase is given by:

$$\langle \mathbf{F}_{DEP} \rangle = \frac{1}{4} \upsilon \,\mathrm{Re}[\tilde{\alpha}] \nabla |\mathbf{E}|^2$$

where υ is the volume of the particle, **E** is the electric field phasor and $\tilde{\alpha}$ is the complex effective polarisability of the particle. This force is the gradient of the energy stored in the induced dipole of the particle and can be positive or negative with respect to that gradient depending on the frequency dependent effective polarisability.

$$U_{DEP} = \frac{1}{4} \upsilon \,\mathrm{Re}[\tilde{\alpha}] |\mathbf{E}|^2$$

Understanding the dielectrophoretic behaviour of a particle requires a solution of the electric field. Trapping regions for particles experiencing positive DEP can be seen in plots of the dielectrophoretic potential (or simply the magnitude of the electric field) as regions of maximum field strength completely enclosed by lower field strength regions. Owing to the nature of electrostatic fields, these will only occur at interfaces or surfaces. Likewise, trapping regions for particles experiencing negative DEP can be seen in plots of the electric field strength as regions of minimum field strength completely enclosed by higher field strength regions.

The electrical problem: electrostatic and quasi-electrostatic

The electrical problem (determining the electric field and from there the dielectrophoretic force) is obtained by solving Maxwell's equations in the electrostatic or quasi-electrostatic approximations. In numerical simulation, approximations are made to obtain the minimum necessary set of equations and conditions for an accurate solution. The electrostatic problem is much simpler than the quasi-electrostatic and is therefore (a) much easier to solve and (b) more accurate as a result.

Electrostatic problems are generally considered to be those where the dielectrics are ideal and the materials only have a permittivity and zero conductivity. As we will discuss later, in the case of water as a non-ideal conducting fluid, the low and high frequency limits (and in fact most of the frequency range barring frequencies close to the charge relaxation frequency) can be solved as electrostatic problems. The electric field is determined by solving Laplace's equation for the potential in a homogeneous material.

$$\nabla \phi = 0 \qquad\qquad \mathbf{E} = -\nabla \phi$$

where ϕ is electrical potential. As long as the boundary conditions hold for the homogeneous material, the solution of the potential and the electric field is dependent only on the geometry of the system and not on the properties of the material.

The more general case of the quasi-electrostatic form of the governing equation can be derived for harmonic electric fields from the field equations

$$\nabla \cdot (\varepsilon \mathbf{E}) = \rho \quad \text{and} \quad \nabla \times \mathbf{E} = 0$$

and the charge conservation equation

$$\frac{\partial \rho}{\partial t} + \nabla \cdot (\sigma \mathbf{E}) = 0$$

where ε is the permittivity of the material, σ is the conductivity and ρ is the free charge density. Combination of these equations gives the quasi-electrostatic form of Poisson's equation

$$\nabla \cdot \left(\varepsilon - \frac{i\sigma}{\omega} \right) \nabla \phi = 0$$

where $\omega = 2\pi f$ is the angular frequency of the electric field. Before performing a numerical simulation, the problem space and boundary conditions must be defined.

Figure S1 shows a schematic diagram of the low and high frequency limiting problem spaces for the problem of electrodes immersed in an aqueous electrolyte. The problem is solved in cylindrical coordinates, defining the origin as the centre of rotation.

The boundary conditions on the electrodes are straightforward fixed potentials. The boundary conditions around the surface of the water can be considered to be Neumann zero current surfaces as shown in Figure S1(a). For the left hand wall, representing the central symmetry axis of the circular trap, this is correct as the zero current boundary is an even symmetry boundary. For the right hand wall, this is a valid approximation since this surface is sufficiently far away as to have no significant effect on the solution of the electrical potential. For the glass-water interfaces (the top and bottom surfaces as shown by the complete cross-section in Figure S1(b)) the correct boundary condition is a consideration of the continuity of normal current i.e.

$$\left(\sigma_{water} - i\omega\varepsilon_{water}\right) \frac{\partial \phi_{water}}{\partial z} = \left(\sigma_{glass} - i\omega\varepsilon_{glass}\right) \frac{\partial \phi_{glass}}{\partial z}$$

Figure S1 Schematic diagram of the two limiting electrostatic problem spaces for an aqueous electrolyte.

(a) at low frequencies, the conductivities of the different materials dominate the polarisation at the water/glass boundary and the problem reduces to the water filled channel and the electrodes.

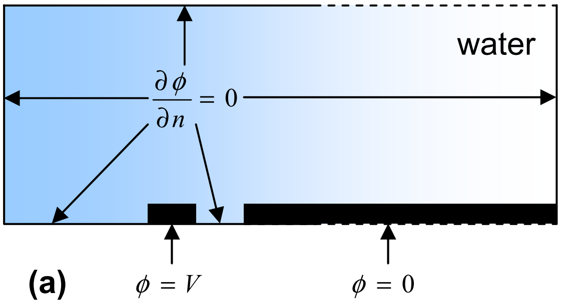

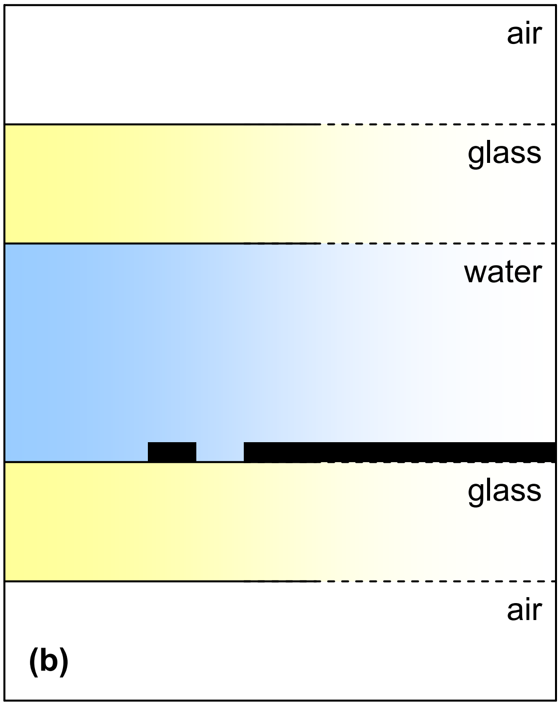

must be true at the interface. At low frequencies, conductivities dominate and this equation reduces to

$$\frac{\partial \phi_{water}}{\partial z} = \frac{\sigma_{glass}}{\sigma_{water}} \frac{\partial \phi_{glass}}{\partial z} = 0$$

Since the conductivity of glass is negligible compared to aqueous electrolytes, for frequencies lower than the charge relaxation frequency σ / ε , the Neumann conditions holds on all glass-water interfaces. At high frequencies, permittivities dominate and this equation reduces to

$$\frac{\partial \phi_{water}}{\partial z} = \frac{\varepsilon_{glass}}{\varepsilon_{water}} \frac{\partial \phi_{glass}}{\partial z} = 0$$

At high frequencies, given the large relative permittivity of water (80) compared to that of glass (~3), the Neumann boundary condition is still a good approximation but correct simulation at high and intermediate frequencies requires that the problem space include the glass sections of the device and the air outside the device (as shown in Figure S1(b)) to sufficient distance that the outer boundaries have no effect on the solution of the potential.

In summary, if the system is operating at frequencies below the charge relaxation frequency, then the field simulation is a simple static solution on the water domain only. It is therefore only a geometric problem as there is only a single homogeneous material to consider and the field solution will be the same regardless of the permittivity and conductivity of the aqueous solution. The ring trap itself is a closed trap due to the circular shape and this region of the field will also be purely geometrical as long as the upper boundary of the water domain is sufficiently far away from the top of the trapping region.

Simulation results

Figure S2 shows the electrical potential and the electric field strength for the two electrostatic cases: low frequency (conductivity dominated) and high frequency (permittivity dominated). The low field trap can be seen at position (0,0) in both plots of the electric field (2(c) and (d)) with the trap closed above it by the curved electric field generated by the ring electrodes. Particles experiencing negative DEP would be trapped in this area are held in a low field region and once the trap is switched on, other particles will be directed away from the trap. In the low frequency static field case shown in Figure S2(c) and (d) there is a second minimum at the top water-glass interface. The field magnitude in this plot is shown on a logarithmic and comparison of the two traps demonstrates that the upper trap is at least two orders of magnitude weaker than the lower trap in the ring. The plots shown in Figures S2(e) and (f) show the difference between the two solutions indicating that the largest difference between the two solutions is at the top of the water chamber near the glass surface. The solution in the region of the ring electrodes and the trap area in the centre show negligible differences. This demonstrates that the upper boundary condition has little effect on the dielectrophoretic trap in the ring and indeed is unlikely to have any effect unless the upper surface is brought down within the trap itself.

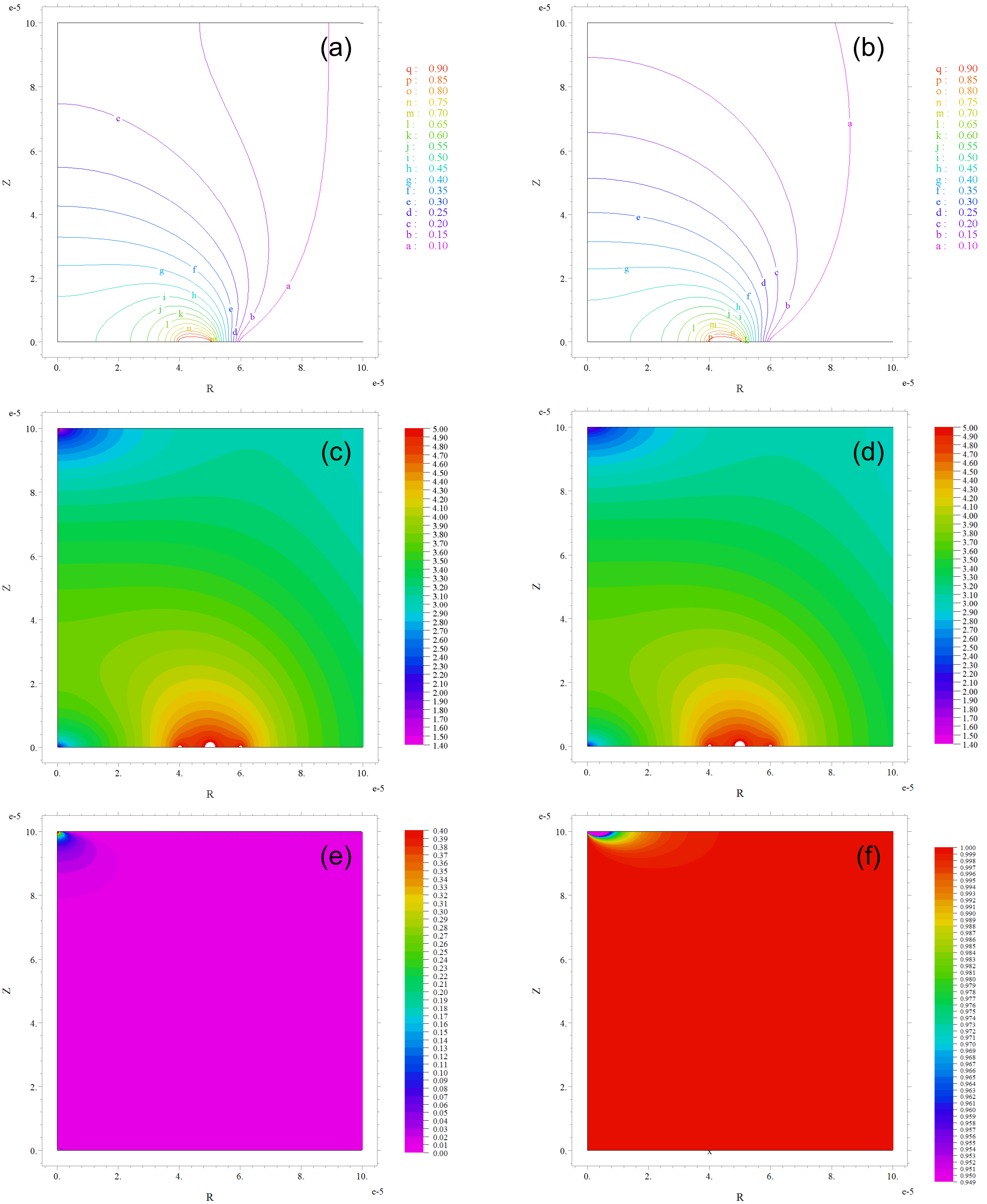

Figure S2. Electrostatic simulations of the electrical potential (a) & (b) and electric field magnitude (c) & (d) for the low (a) & (c) and high (b) & (d) frequency limits. The field magnitude is plotted on a log base 10 scale in order to visualise the large range of orders of magnitude, with the highest values of the electric field found at the edges of the electrodes (40, 50 and 60 µm). The negative DEP trap can be seen in the bottom left hand corner (the centre of the trap) and a second, weaker trap can be seen at the top glass interface. Plots of the difference between (e) the magnitude of and (f) the divergence between the electric field calculated for the low and high frequency electrostatic cases. The differences are greatest near the top of the water chamber and negligible at the bottom.

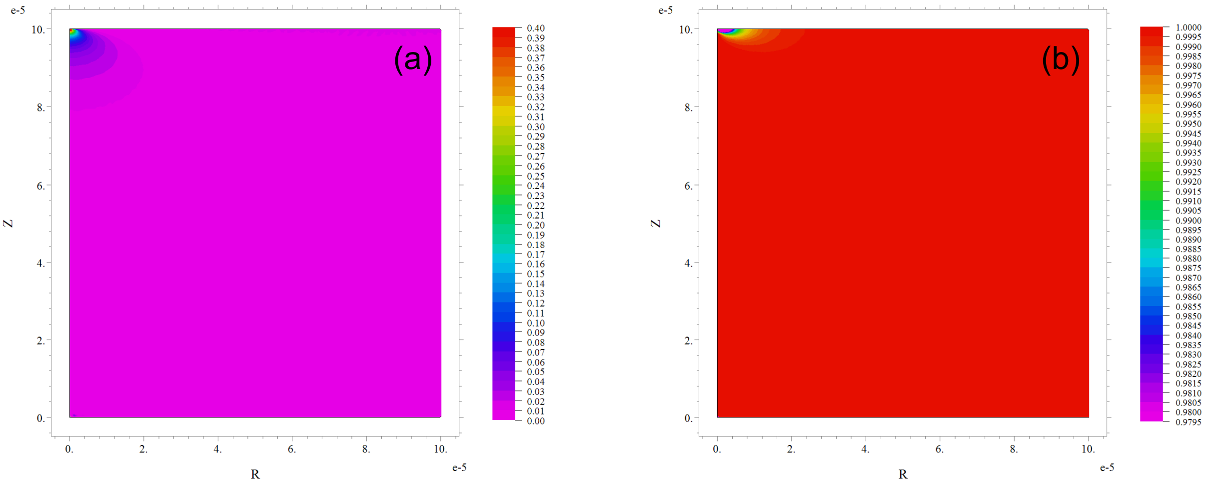

Figure S3. Plots of the difference between (a) the magnitude of and (b) the divergence between the electric field calculated for the low frequency electrostatic case and the experimental electrolyte conductivity of 1.9mS/m and 1MHz. The differences are greatest near the top of the water chamber and negligible at the bottom.

Figure S4. Plots showing the magnitude of the electric field in the radial direction at a height of 7.5µm. (a) the values for the high frequency static simulation including the glass and air sections compared with the low frequency static value calculated for only the water chamber containing the electrodes. (b) and (c) the values for 1.9mS/m at low frequencies and the experimental frequency of 1MHz are compared with the low frequency static solution. (d) and (e) the values for 1.6S/m at low frequencies and the experimental frequency of 20MHz are compared with the low frequency static solution.

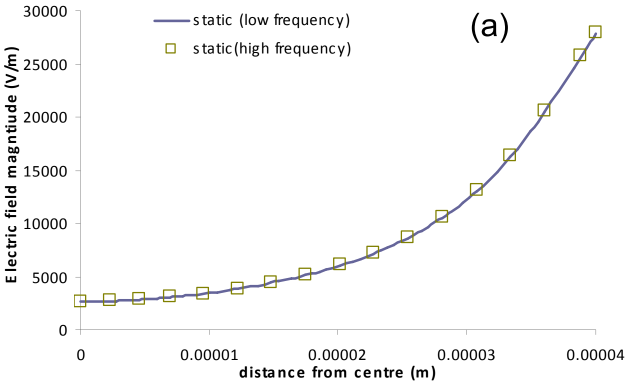

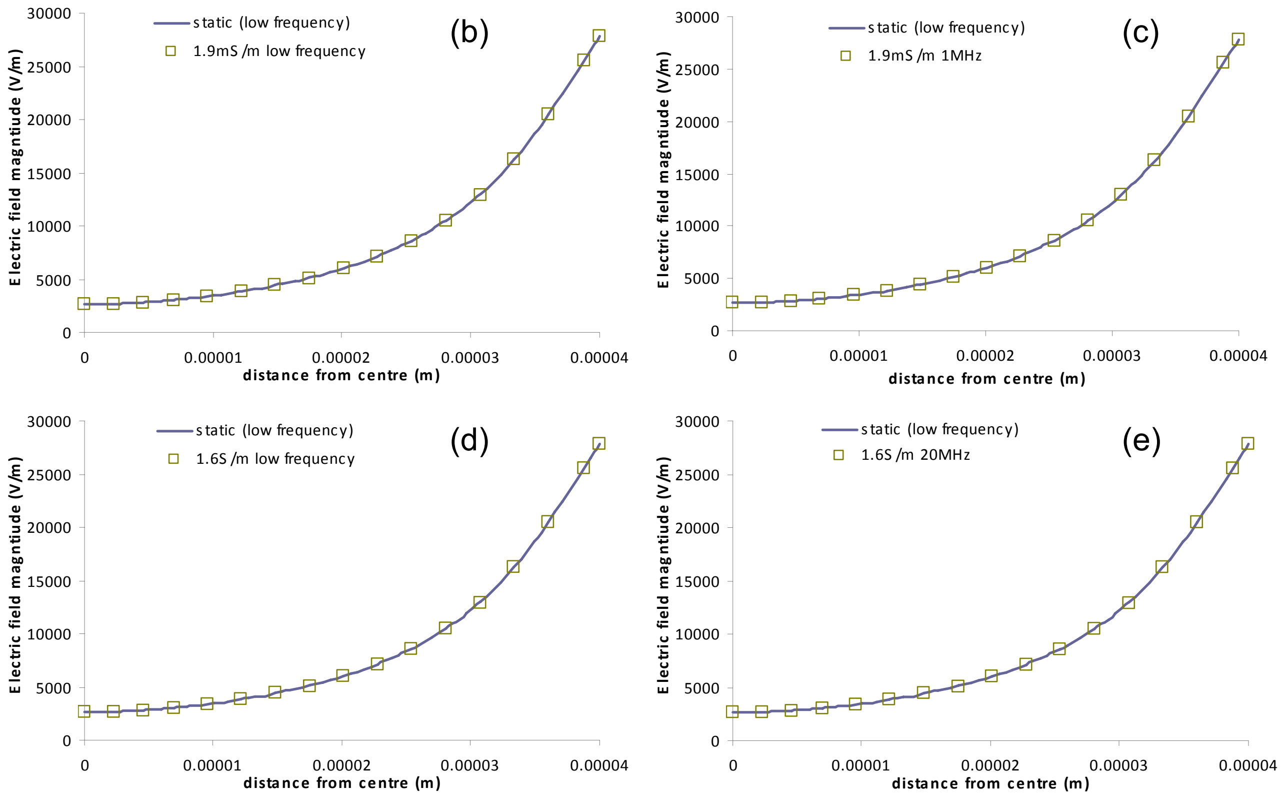

Figure S5. Plots showing the magnitude of the dielectrophoretic force component in the radial direction at a height of 7.5µm. (a) the values for the high frequency static simulation including the glass and air sections compared with the low frequency static value calculated for only the water chamber containing the electrodes. (b) and (c) the values for 1.9mS/m at low frequencies and the experimental frequency of 1MHz are compared with the low frequency static solution. (d) and (e) the values for 1.6S/m at low frequencies and the experimental frequency of 20MHz are compared with the low frequency static solution.

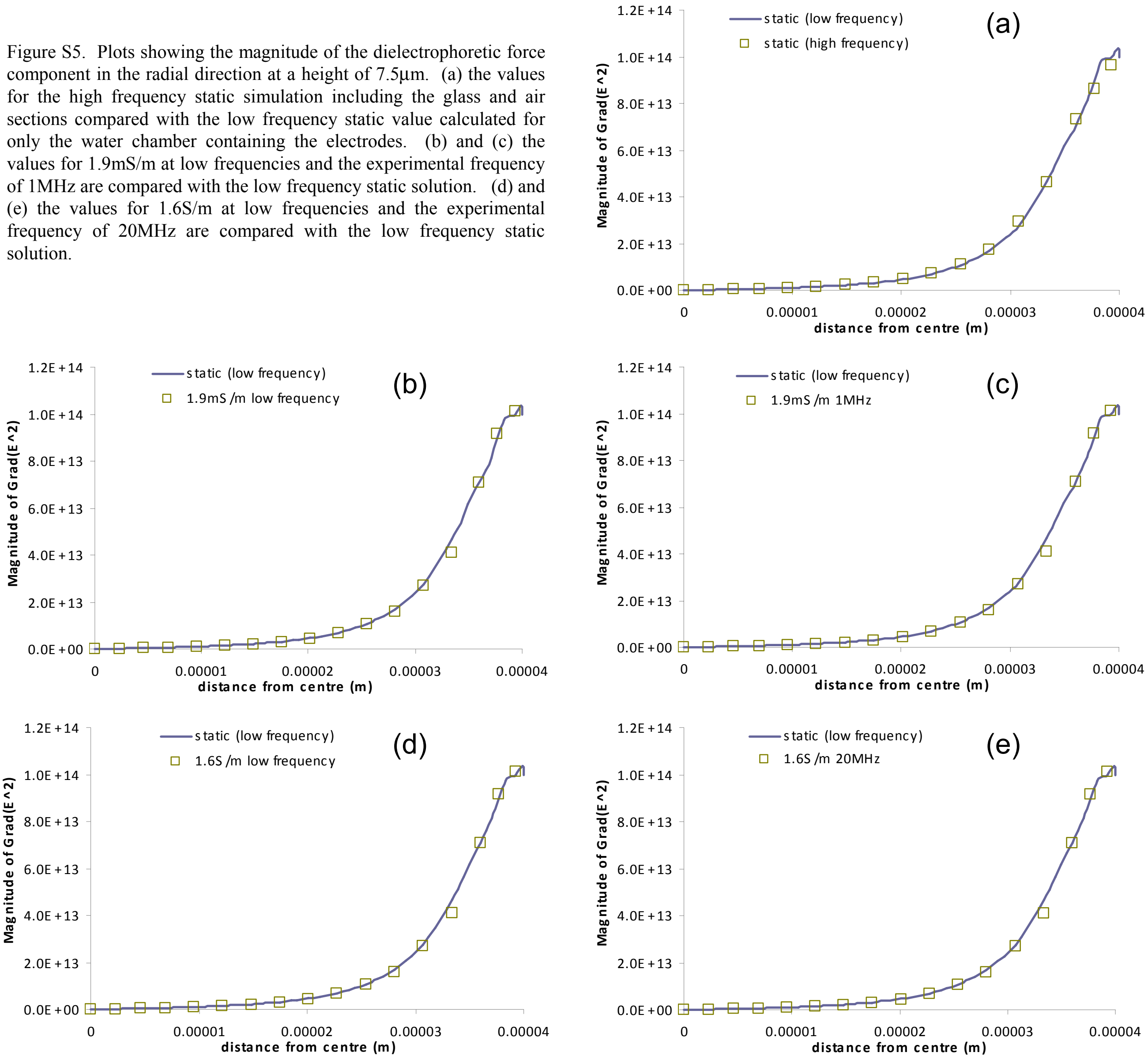

Next, typical example experimental conditions from the paper were simulated ussing the full frequency dependent quasi-electrostatic equations. For the 1.9mS/m electrolyte a simulation at 1Hz to check the low frequency solution and a simulation at the experimental frequency of 1MHz were performed. For the 1.6S/m electrolyte simulations were performed at 1Hz and 20MHz.

Figures S4 and S5 show the electric field strength and the trapping force (at 7.5 µm for the approximate height of the particle in the main text) for the four experimental conditions and the high frequency electrostatic simulation. In each case, the results are compared with the low frequency electrostatic simulation demonstrating agreement within the numerical error in the simulation. The trapping force increases out to the edge of the trap over the electrode edge and has a minimum value in the centre. The good agreement in each case demonstrates that the trapping field in the centre is a purely geometrical shape arising from the design of the electrodes.

As a result, over a wide range of frequencies and medium conductivities, the electrostatic calculation of the trapping force is a valid result. Simulation of this problem is significantly easier than the quasi-electrostatic problem and can therefore be calculated to a much higher degree of precision.

Two ring device results

Figure S6 shows the electric field calculated for the device consisting of two rings. The field profile is largely the same, with the same two traps at the glass surfaces. The field is slightly weaker for the same applied potential but is more localised to the electrodes themselves. Figure S7 shows a direct comparison of the field and the DEP force at the reference height of 7.5µm, demonstrating a roughly 20% decrease.

Current and Impedance calculations

Two different field parameters must be calculated in order to determine the impedance of the device. The first is the current which can be found from the integral of the normal field across a surface which intersects all lines of current, for example the two electrodes, multiplied by the conductivity of the solution. The resistance is then found by dividing the applied volatge by the current:

$$R = \frac{V}{\int_S J_n ds} = \frac{V}{\int_S \sigma E_n ds}$$

The capacitance is then determined from the energy stored in the system, which can be found by integrating the static energy density across the whole simulated volume. The capacitance is then found from the energy as:

$$C = \frac{1}{V^2}\int_v \mathbf{E}\cdot\mathbf{D}d\upsilon = \frac{\varepsilon}{V^2}\int_v |\mathbf{E}|^2 d\upsilon$$

The value for capacitance and resistance calculated from the field simulations are shown in Table S1.

Table S1 Comparison of resistance and capacitance

Device type and conditions	Resistance	Capacitance
Ring-plane (unscaled)	$R = \frac{1}{\sigma \times 2.91 \times 10^{-4}}$	$C = \varepsilon \times 2.96 \times 10^{-4}$
1.9mS/m	1.81M Ω	0.21pF
1.6S/m	2150Ω	0.21pF
Ring-ring (unscaled)	$R = \frac{1}{\sigma \times 2.55 \times 10^{-4}}$	$C = \varepsilon \times 2.58 \times 10^{-4}$
1.9mS/m	2.06M Ω	0.183pF
1.6S/m	2451Ω	0.183pF

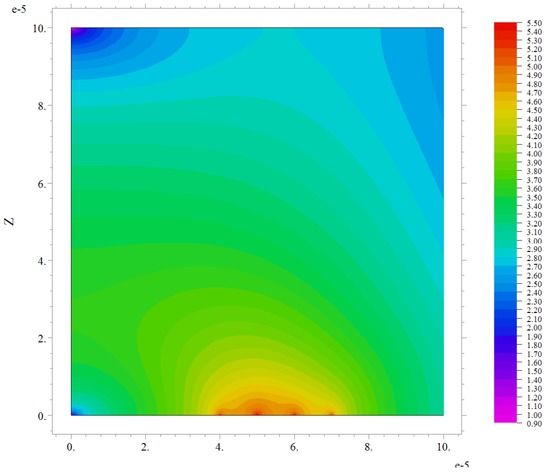

Figure S6 Electric field simulated for the device consisting of two concentric rings. The field magnitude is plotted on a log base 10 scale, with the highest values of the electric field found at the edges of the electrodes (40, 50, 60 and 70 µm).

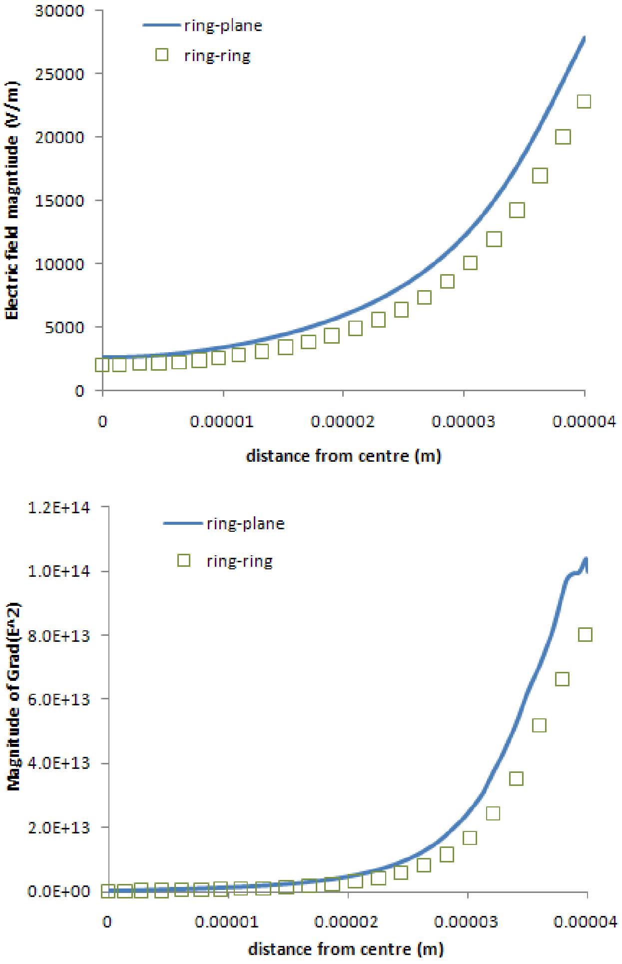

Figure S7 Comparison of the magnitude of (a) electric field and (b) the dielectrophoretic force component in the radial direction at a height of 7.5µm for the two designs of electrode.

Thermal simulation

The thermal field is a solution of the energy balance equation

$$\rho_m c_p \frac{\partial T}{\partial t} + \rho_m c_p \mathbf{u} \cdot \nabla T = k\nabla^2 T + \sigma \frac{1}{2}|\mathbf{E}|^2$$

where c_p is the specific heat at constant pressure, k is the thermal conductivity and the last term on the right hand side is the Joule heating term. We are only interested in the steady state solution and neglect the first term on the left-hand side. Also, the ratio of natural heat convection to heat diffusion is very small: the Grashof number is calculated to be much smaller than 1. The temperature is therefore governed simply by the diffusion equation

$$k\nabla^2 T + \sigma \frac{1}{2}|\mathbf{E}|^2 = 0$$

The problem space consists of the water and glass substrate and lid. Two experimental setups were simulated, with the device either sitting on a metal heat sink or sitting on a peltier cooler. The top surface of the problem space was set to a constant temperature (room temperature – 20°C). The bottom surface of the glass substrate was set either to room temperature or to 4°C to simulate the effect of a cooled heat sink. The thermal conductivities of the glass and the water are 1.0 and 0.6 respectively. The left-hand boundary (the centre of the trap) was assigned to be a plane of even symmetry. The right hand edge of the simulation domain was assigned to be a linear function of the temperature varying from the top surface value to the bottom surface value.

One simulated result in the region of the trap is shown in Figure S8 for an applied signal of potential 5 V pk-pk in an electrolyte of conductivtiy 1.6 S/m. The maximum temperature in the domain represents a temperature rise of 0.59°C over the ambient temperature due to Joule heating in the fluid. This hot region is not suprisingly over the electrode where the electric field is the strongest. The temperature rise in the centre of the trap is 0.46°C, with the central region of the trap warmer than the surroundings. Figure S9 shows plots of the temperature in the centre of the trap and the maximum temperature in the domain as a function of voltage for the two experimental setups. The temperature increase is proportional to voltage squared. At 10 V pk-pk the temperature in the trap is 30°C (a rise of 10°C) and for 20 V pk-pk the rise is over 40°C. The use of the cooled heat sink on the lower surface has the effect of reducing the ambient temperature in the trap by approximately 9°C, meaning that at 10 V pk-pk the temperature can be maintained at 20°C but not for higher voltages. However, if the ambient temperature was required to be maintained at 37°C, higher voltages can be used. In lower conductivities, the temperature rises are negligible.

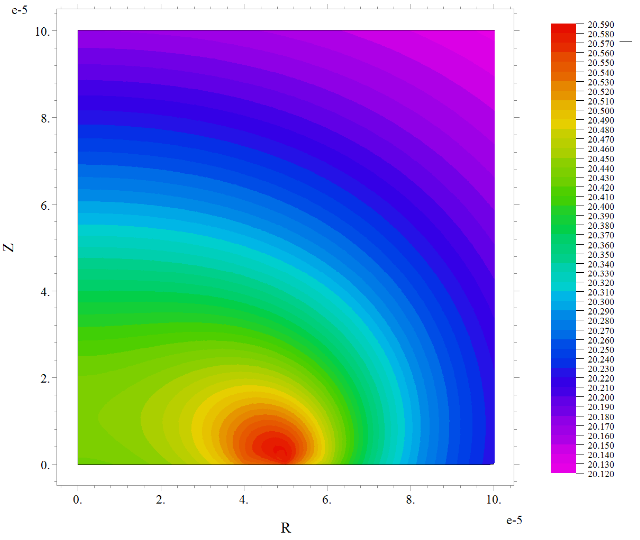

Figure S8 Simulated thermal field for an applied voltage of 5volts peak to peak in a solution of conductivity 1.6S/m. The highest temperature in this case was 20.59°C, found over the electrode (40–50µm) with a lower but still raised temperature in the centre of the trap.

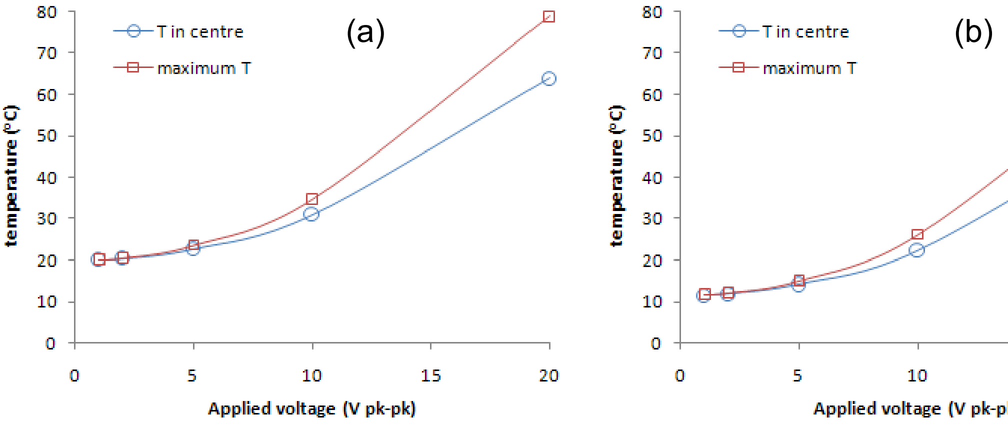

Figure S9 Plots of the temperature in the centre of the trap and the maximum temperature in the array calculated as a function of applied voltage for (a) room temperature boundary conditions and (b) a lower boundary condition of 4°C, with an electrolyte conductivity of 1.6S/m. The temperature is proportional to voltage squared as expected.

References

S1 A.Ramos, H.Morgan, N.G.Green and A.Castellanos, *J. Phys. D: Appl. Phys.,* 1998, **31**, 2338

S2 N.G. Green, A. Ramos, A. González, A. Castellanos and H. Morgan, *Journal of Electrostatics*, 2001, **53**, 71

S3 N.G. Green, A. Ramos and H. Morgan, *Journal of Electrostatics*, 2002, **56**, 235

S4 J.A. Stratton, Electromagnetic Theory, McGraw-Hill, New York, 1941.

S5 J.R. Melcher Continuum Electromechanics, MIT Press, Cambridge, USA, 1981.

S6 D.R. Lide (editor) CRC Handbook of Chemistry and Physics. 74th edition, CRC Press, London, 1994.

S7 A. Castellanos, Electrohydrodynamics (ed. A. Castellanos), Springer-Verlag, Wien, NewYork, 1998.

S8 N.G. Green, A. Ramos A. González, A. Castellanos and H. Morgan, *J. Phys. D: Appl. Phys.,* 2000, **33**, L13

S9 A. González, A. Ramos, H. Morgan, N.G. Green and A. Castellanos, *Journal of Fluid Mechanics*, 2006, **564**, 415